A Fully Compressible Nonhydrostatic Deep-Atmosphere Equations Solver for MPAS

WILLIAM C. SKAMAROCK,[a] HING ONG,[b] AND JOSEPH B. KLEMP[a]

[a] *National Center for Atmospheric Research, Boulder, Colorado*
[b] *University of California, Davis, Davis, California*

(Manuscript received 31 August 2020, in final form 4 December 2020)

ABSTRACT: A solver for the nonhydrostatic deep-atmosphere equations of motion is described that extends the capabilities of the Model for Prediction Across Scales-Atmosphere (MPAS-A) beyond the existing shallow-atmosphere equations solver. The discretization and additional terms within this extension maintain the C-grid staggering, hybrid height vertical coordinate, and spherical centroidal Voronoi mesh used by MPAS, and also preserve the solver's conservation properties. Idealized baroclinic wave test results, using Earth-radius and reduced-radius sphere configurations, verify the correctness of the solver and compare well with published results from other models. For these test cases, the time evolution of the maximum horizontal wind speed, and the total energy and its components, are presented as additional solution metrics that may allow for further discrimination in model comparisons. The test case solutions are found to be sensitive to the configuration of dissipation mechanisms in MPAS-A, and many of the differences among models in previously published test case solutions appear to arise because of their differing dissipation configurations. For the deep-atmosphere reduced-radius sphere test case, small-scale noise in the numerical solution was found to arise from the analytic initialization that contains unstable lapse rates in the tropical lower troposphere. By adjusting a parameter in this initialization, the instability is removed and the unphysical large-scale overturning no longer occurs. Inclusion of the deep-atmosphere capability in the MPAS-A solver increases the dry dynamics cost by less than 5% on CPU-based architectures, and configuration of either the shallow- or deep-atmosphere equations is controlled by a simple switch.

KEYWORDS: Coordinate systems; Grid systems; Model comparison; Nonlinear models; Numerical analysis/modeling; Vertical coordinates

1. Introduction

Nonhydrostatic global models have typically been developed to integrate the equations of motion in which the shallow-atmosphere approximation is employed (see e.g., White et al. 2005, for an overview of this and other approximations). This approximation, used in most operational weather prediction and climate models, has proven accurate for applications where the necessary solution fidelity extends into the mid–upper stratosphere. For applications requiring model tops extending through the mesosphere into the lower thermosphere, the shallow-atmosphere approximation becomes significantly less accurate (e.g., White and Bromley 1995; Akmaev 2011). Since the depth of the atmospheric domain is no longer negligible in comparison to Earth's radius, the deep-atmosphere equations typically take into account the r^{-2} variation of gravity, where r is the radial distance from the center of Earth, as well as variation of the mesh geometry, where horizontal lengths and areas scale with r and r^2, respectively. In addition, for quasi-hydrostatic and nonhydrostatic models, the full Coriolis terms are warranted as there are studies suggesting that the neglect of the full Coriolis terms may lead to significant errors in the tropics (e.g., Hayashi and Itoh 2012; Ong and Roundy 2019, 2020a).

Geospace applications use model tops in excess of 500 km, well into the mesosphere and ionosphere, where the accuracy of the shallow-atmosphere approximation is even more problematic. Nonetheless, it is interesting that most of the mesosphere–ionosphere models that have been developed over the years have been based on the shallow-atmosphere primitive equations, with additional physical processes included that are appropriate for the thermosphere and ionosphere. Examples include the Thermosphere General Circulation Model (TGCM; Dickinson et al. 1981), the Thermosphere–Ionosphere General Circulation Model (TIGCM; Roble et al. 1988), the Coupled Middle Atmosphere and Thermosphere (CMAT) general circulation model (Harris et al. 2002), and the Whole Atmosphere Community Climate Model (WACCM; Liu et al. 2018). An exception is the Global Ionosphere–Thermosphere Model (GITM; Ridley et al. 2006), which solves the full deep-atmosphere nonhydrostatic equations.

Over the last two decades a number of nonhydrostatic atmospheric models used in weather and climate applications have been modified to integrate the deep-atmosphere equations that accommodate the generalizations mentioned above. These models include, for example, one of the earliest global nonhydrostatic models NICAM (Satoh et al. 2008), the Met Office model ENDGAME (Wood et al. 2014) and the research model MCore (Ullrich et al. 2014, and references therein), and the ICON model (Borchert et al. 2019). Although very few tests exist to validate deep-atmosphere equations solvers, all these models except NICAM (unreported) were evaluated with a baroclinic wave test case (Ullrich et al. 2014), where shallow and deep configurations are tested on spheres of both Earth radius and a reduced radius. The simulated baroclinic waves behave similarly in these tests except for the deep-atmosphere reduced-radius case, and previous studies did not

Corresponding author: William C. Skamarock, skamaroc@ucar.edu

DOI: 10.1175/MWR-D-20-0286.1

explain why this case stands out. It is unlikely that the behavior is due to the additional Coriolis and curvature terms because the strong stratification of entropy needed by the baroclinic waves theoretically makes the nontraditional Coriolis terms unimportant (Müller 1989), and the curvature terms are even smaller. In addition to the baroclinic wave test, Borchert et al. (2019) proposed an acoustic wave test, but it is less useful for models that handle acoustic waves anisotropically. In giant planet studies, for example, Glatzmaier et al. (2009), Heimpel et al. (2005), and Verhoeven and Stellmach (2014) have reported many numerical simulations using the deep-atmosphere equations, but these simulations were not designed for validating numerical weather prediction models. In these giant planet studies, under weak stratification, the inclusion of the nontraditional Coriolis terms makes vortices parallel to the axis of planet rotation instead of vertical. Thus, Ong and Roundy (2020b) proposed an initial value problem with a linearized analytical solution simulating axis-parallel vortices under isentropic condition, and used it to validate the implementation of nontraditional Coriolis terms in MPAS-A. However, the analytical solution does not account for spherical geometry.

In this paper we describe the extension of the Model for Prediction Across Scales-Atmosphere (MPAS-A; Skamarock et al. 2012) dynamical core modifying it to integrate either the shallow- or deep-atmosphere equations. MPAS-A uses a finite-volume discretization of the equations of motion and a spherical centroidal Voronoi tessallation (SCVT) for its horizontal mesh, in addition to the C-grid staggering. Collectively these features represent a unique configuration among the nonhydrostatic global models that employ the deep-atmosphere equations. The finite-volume formulation for the deep-atmosphere equations in the height coordinates used in MPAS-A is straightforward, and we describe the extension to the MPAS-A solver in section 2. There are few idealized test cases for the deep-atmosphere equations, and in section 3 we test the MPAS-A solver with the baroclinic wave tests for the Earth-radius sphere used in Ullrich et al. (2014), where we also present additional solution metrics and model configuration results. In section 4 we examine baroclinic wave solutions for the reduced-radius sphere test case also introduced in Ullrich et al. In conducting these tests, we found that unstable lapse rates were present in the initial lower tropical troposphere for the reduced-radius sphere deep-atmosphere case. After suitably removing this initial instability, we present modified results in section 4 that are in much closer agreement with the shallow-atmosphere results. Section 5 summarizes the results and discusses the limitations of the test cases.

2. Formulation

MPAS-A (Skamarock et al. 2012) uses a finite volume discretization of the shallow-atmosphere equations in addition to a spherical centroidal Voronoi mesh and a C-grid staggering of the prognostic variables. MPAS uses the standard formulation of the shallow-atmosphere approximation (White and Bromley 1995). With spherical geometry, the shallow-atmosphere equations with the complete Coriolis terms and a simple modification can conserve an approximated form of angular momentum (Tort and Dubos 2014). However, to conserve angular momentum in its standard form, the deep-atmosphere geometry is necessary for the nontraditional Coriolis terms (White and Bromley 1995).

Other atmospheric models that have been extended to solve the deep-atmosphere equations also use finite volume discretizations and similar meshes. The NICAM model (Satoh et al. 2008) employs an icosahedral mesh with no staggering of the prognostic variables (i.e., an A-grid). It also uses an energy-conserving time-integration scheme based on Satoh (2002), which differs from that used in MPAS. Borchert et al. (2019) describe the deep-atmosphere extension of the ICON model employing C-grid staggered prognostic variables on a triangular icosahedral mesh, essentially the dual of the MPAS Voronoi mesh. With regard to geometry our deep-atmosphere formulation closely follows that used in the ICON model except for the horizontal mesh.

a. Continuous equations

The MPAS atmosphere solver, described in Skamarock et al. (2012), employs a height-based terrain-following vertical coordinate ζ following Klemp (2011). The coupled prognostic variables in this coordinate are defined as

$$\tilde{\rho}_d = \frac{\rho_d}{\zeta_z}, \tag{1}$$

$$\mathbf{V}_H = \tilde{\rho}_d \mathbf{v}_H, \tag{2}$$

$$W = \tilde{\rho}_d w, \tag{3}$$

$$\Theta_m = \tilde{\rho}_d \theta \left[1 + \left(\frac{R_v}{R_d}\right) q_v\right], \tag{4}$$

$$Q_j = \tilde{\rho}_d q_j, \tag{5}$$

where the vertical derivative of the computational coordinate $\zeta_z = \partial\zeta/\partial z$, ρ_d is the dry-air density, $\mathbf{v}_H$ and w represent the horizontal and vertical velocities ($u\mathbf{i}$, $v\mathbf{j}$, $w\mathbf{k}$) where $\mathbf{i} \times \mathbf{j} = \mathbf{k}$, θ is the potential temperature, q_v is the water vapor mixing ratio with respect to the dry-air density ρ_d, q_j are the mixing ratios of other moisture constituents and other scalars, and R_d and R_v are the gas constants for dry air and water vapor, respectively. The full continuous equations for both deep- and shallow-atmosphere configurations can be cast as

$$\frac{\partial \mathbf{V}_H}{\partial t} = -\frac{\rho_d}{\rho_m}\left[\nabla_\zeta\left(\frac{p}{\zeta_z}\right) + \frac{\partial}{\partial\zeta}\left(\frac{\zeta_H p}{\zeta_z}\right)\right] - \eta\,\mathbf{k}\times\mathbf{V}_H - \mathbf{v}_H\nabla_\zeta\cdot\mathbf{V} - \frac{\partial \Omega \mathbf{v}_H}{\partial\zeta} - \tilde{\rho}_d\nabla_\zeta K + \mathbf{F}_{V_H} - \beta_d\tilde{\rho}_d\left(ew\mathbf{i} + \frac{\mathbf{v}_H w}{r}\right), \tag{6}$$

$$\frac{\partial W}{\partial t} = -\frac{\rho_d}{\rho_m}\left[\frac{\partial p}{\partial\zeta} + g\left(\frac{r_o}{r}\right)^2\tilde{\rho}_m\right] - (\nabla\cdot\mathbf{v}\,W)_\zeta + F_W + \beta_d\tilde{\rho}_d\left(\frac{\mathbf{v}_H\cdot\mathbf{v}_H}{r} + e\mathbf{v}_H\cdot\mathbf{i}\right), \tag{7}$$

$$\frac{\partial \Theta_m}{\partial t} = -(\nabla\cdot\mathbf{V}\,\theta_m)_\zeta + F_{\Theta_m}, \tag{8}$$

$$\frac{\partial \tilde{\rho}_d}{\partial t} = -(\nabla \cdot \mathbf{V})_\zeta, \tag{9}$$

$$\frac{\partial Q_j}{\partial t} = -\left(\nabla \cdot \mathbf{V} q_j\right)_\zeta + F_{Q_j}. \tag{10}$$

The term $\beta_d = 1$ for the deep-atmosphere equations, and the traditional shallow-atmosphere approximation is recovered when $\beta_d = 0$ and the radial distance from the center of the sphere r is approximated by the constant sphere radius r_o. The gravity g is defined by its value at the sphere surface. The horizontal momentum equation (6) is not cast in conservative (flux) form. In (6) the absolute vertical vorticity $\eta = \mathbf{n} \cdot \nabla \times \mathbf{v}_H + f$, where $\mathbf{n}$ is the unit vector normal to a ζ surface, and $\mathrm{K} = |\mathbf{v}_H|^2/2$ is the horizontal kinetic energy. In the curvature and Coriolis terms in (6) and (7), $f = 2\Omega_e \sin\psi$, $e = 2\Omega_e \cos\psi$, ψ is the latitude, Ω_e is the angular rotation rate of Earth. The terms $\mathbf{F}_{V_H}$, F_W, F_{Θ_m}, and F_{Q_j} represent sources and sinks from physics, subgrid models, and filters. The mass-flux normal to the horizontal coordinate surface is $\Omega = \mathbf{V} \cdot \nabla\zeta$ and the corresponding normal velocity is $\omega = \dot{\zeta}$.

b. Discrete equations

The MPAS solver uses a spherical centroidal Voronoi mesh and a C-grid finite-volume discretization. All prognostic variables are defined as cell (volume) averaged variables except for the velocities that are defined as area averages of the face-normal velocities over the cell faces.

To accommodate the deep-atmosphere geometry in the MPAS finite-volume discretization, we begin by considering the conservation equations for the cell averaged variables, i.e., Θ_m, ρ_d, Q_j. The finite volume discretization for these variables is derived by integrating the conservation equation over the cell volume and using the divergence theorem to express the volume integral of the flux divergence as an area integral of the fluxes through the cell faces. The discrete conservation equation for an arbitrary scalar mass $\rho_d b$ for the shallow-atmosphere equations is

$$\frac{\partial(\tilde{\rho}_d b) A_o \Delta\zeta}{\partial t} = -\sum_{\text{edges}} (U \cdot \mathbf{n}) \overline{b}^e l_e \Delta\zeta - \left[(\Omega \overline{b}^\zeta A_o)^{\zeta+\frac{\Delta\zeta}{2}} - (\Omega \overline{b}^\zeta A_o)^{\zeta-\frac{\Delta\zeta}{2}}\right], \tag{11}$$

where $\mathbf{n}$ is the unit normal directed outward from the edge for the cell, and $\overline{b}^e$ and $\overline{b}^\zeta$ represent transport scheme stencils projecting the quantity b to the cell edges (see Skamarock and Gassmann 2011). Dividing through by the volume $A_o\Delta\zeta$ casts (11) in the form directly integrated in the model:

$$\frac{\partial(\tilde{\rho}_d b)}{\partial t} = -\frac{1}{A_o}\sum_{\text{edges}} (U \cdot \mathbf{n}) \overline{b}^e l_e - \frac{1}{\Delta\zeta}\left[(\Omega \overline{b}^\zeta)^{\zeta+\frac{\Delta\zeta}{2}} - (\Omega \overline{b}^\zeta)^{\zeta-\frac{\Delta\zeta}{2}}\right]. \tag{12}$$

The term $(U \cdot \mathbf{n})$ is the horizontal mass flux normal to the cell edge in (11) and (12), with an outward flux being positive, and the horizontal area of a cell A_o and the length of a cell edge as l_e are defined on the surface of the sphere as the spherical area of the cell and the great-circle length between vertices on the sphere surface, respectively.

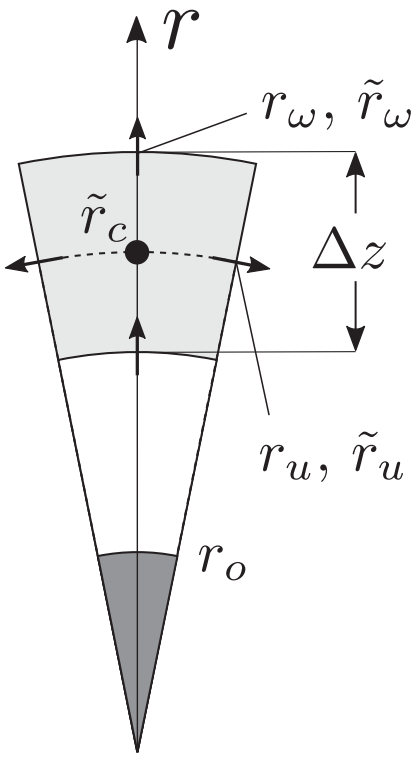

FIG. 1. Schematic of a vertical cross section through an MPAS mesh cell employed in the deep-atmosphere solver. The surface of the sphere is at $r = r_o$, and the dark shaded area represents the interior of the sphere.

For the deep-atmosphere equations, the cell volume and the cell face areas are now functions of the radius from the center of the sphere. A schematic of a vertical cross section through a cell for the deep-atmosphere mesh is depicted in Fig. 1. For the horizontal cell areas through which vertical fluxes are defined (i.e., where the vertical velocities w and ω are prognosed at radius r_ω in Fig. 1), the cell face area scales with the radius squared:

$$A_\omega = A_o\left(\frac{r_\omega}{r_o}\right)^2. \tag{13}$$

For the vertical cell-edge faces through which the horizontal fluxes are defined, the cell-edge face area is

$$A_u = \int_{r_1}^{r_2} l_e \frac{r}{r_o} dr = \frac{l_e}{r_o}\frac{(r_2 - r_1)(r_2 + r_1)}{2} = l_e \Delta z\left(\frac{r_u}{r_o}\right), \tag{14}$$

where r_u is the radius at the u point that lies at the vertical midpoint of the cell-edge face on the MPAS mesh, and the integration limits r_1 and r_2 are from the bottom to the top of the cell at that edge face. Finally, the cell volume is

$$V_{\text{cell}} = \int_{r_1}^{r_2} A_o \frac{r^2}{r_o^2} dr, = \frac{A_o}{3r_o^2}(r_2^3 - r_1^3) = A_o \Delta z\left(\frac{r_1^2 + r_1 r_2 + r_2^2}{3r_o^2}\right), \tag{15}$$

The cell volume (15) is identical to Eq. (14) in Borchert et al. (2019) describing the deep-atmosphere formulation for the ICON model that uses a triangular mesh (the dual of the Voronoi mesh) and also uses a finite-volume formulation for the cell-centered variables. The adjustments to the cell-face areas (13) and (14) are also identical to Borchert et al. (2019), as given in their Eqs. (16) and (15), respectively.

In most applications the integration of the cell-based conservation equations is the most costly component in the dynamics, and we seek to minimize the extra computations associated with these integrations in a deep-atmosphere implementation. We can retain the same discrete form (12) for these cell-based conservation equations by redefining the coupled density and momentum variables (1), (2), and (3) as

$$\tilde{\rho}_d = \frac{\rho_d \tilde{r}_c^2}{\zeta_z}, \tag{16}$$

$$\mathbf{V}_H = \overline{\left(\frac{\tilde{\rho}_d}{\tilde{r}_c^2}\right)}^{e} \mathbf{v}_H \tilde{r}_e, \tag{17}$$

$$\Omega = \overline{\left(\frac{\tilde{\rho}_d}{\tilde{r}_c^2}\right)}^{\zeta} \omega \tilde{r}_\omega^2. \tag{18}$$

The coupled potential temperature (4) and scalars (5) retain their form but now use the redefined coupled density (16) in their definitions. These additional scaling factors $\tilde{r}_c$, $\tilde{r}_e$, and $\tilde{r}_\omega$ are defined at the cell centers, cell edges, and cell interfaces, respectively, where $\tilde{r}_e = r_u/r_o$, $\tilde{r}_\omega = r_\omega/r_o$, and

$$\tilde{r}_c^2 = \frac{r_1^2 + r_1 r_2 + r_2^2}{3 r_o^2},$$

for the deep-atmosphere geometry. For the shallow atmosphere $r = r_o$ and $\tilde{r}_c$, $\tilde{r}_e$, and $\tilde{r}_\omega$ equal 1. Thus the scaling of the density and momentum in the shallow-atmosphere formulation are now augmented by an additional metric terms to account for the deep-atmosphere mesh geometry as represented in (16)–(18), and cast in such a way that the conservation equations for the cell-based variables, and importantly their flux divergence operators, are unchanged in the solver.

In contrast, some of the discrete operators in the momentum equations need to be directly modified to incorporate the deep-atmosphere geometry. Specifically, the discrete operators for the pressure gradient and for the relative vorticity needed in the horizontal momentum equation (6) are now cast as

$$\nabla_\zeta b\Big|_{\text{edge}} = \frac{1}{\tilde{r}_e} \nabla_{\zeta_o} b\Big|_{\text{edge}} = \frac{b_2 - b_1}{\tilde{r}_e d_e}, \tag{19}$$

and

$$\mathbf{n} \cdot \nabla \times \mathbf{v}_H = \frac{1}{\tilde{r}_\nu^2 A_\nu} \sum_{\text{edges}} u_e d_e \tilde{r}_e, \tag{20}$$

where the horizontal lengths between cell centers d_e and the area of the triangle centered over cell vertices A_ν are given at the surface of the sphere.

Given the definitions (19) and (20), we can write the discrete version of the horizontal momentum Eq. (6), cast in terms of the cell-face normal momentum U, as

$$\begin{aligned}\frac{\partial U}{\partial t} = &-\tilde{r}_e \overline{\left(\frac{\rho_d}{\rho_m}\right)}^{e} \left[\frac{1}{\tilde{r}_e}\frac{1}{\zeta_z}\left(\frac{\partial p}{\partial x}\right)_{\zeta_o} + \overline{\left(\frac{\tilde{\rho}_m}{\tilde{r}_c^2}\right)}^{e} g \frac{1}{\tilde{r}_e^3}\left(\frac{\partial z}{\partial x}\right)_{\zeta_o}\right] - \tilde{r}_e \eta \overline{\left(\frac{\tilde{\rho}_d}{\tilde{r}_c^2}\right)}^{e} v \\ &- \frac{1}{\tilde{r}_e}\left(u \nabla_\zeta \cdot \mathbf{V} + \frac{\partial \Omega u}{\partial \zeta}\right) - \overline{\left(\frac{\tilde{\rho}_d}{\tilde{r}_c^2}\right)}^{e} \left(\frac{\partial K}{\partial x}\right)_{\zeta_o} + \tilde{r}_e F_U \\ &- \beta_d \frac{\overline{\tilde{\rho}_d}^{e}}{\tilde{r}_e}\left[e \overline{\overline{w}^{\zeta}}^{e} \cos\alpha_r + \frac{u \overline{\overline{w}^{\zeta}}^{e}}{\tilde{r}_e r_o}\right],\end{aligned} \tag{21}$$

where in the local coordinate (x, y) the x direction is normal to the cell edge, y is parallel to the edge and follows the right-hand rule, α_r is the rotation angle between the line normal to the horizontal velocity (using a right-hand rule) and the meridian, and the local horizontal velocity components are (u, v). The edge-tangent velocity v is diagnosed as described in Thuburn et al. (2009). In the discrete formulation (21) we approximate the metric term in the horizontal pressure gradient within the horizontal momentum equation (6) (the first term in brackets) by its hydrostatic value:

$$\frac{\partial(\zeta_x p)}{\partial \zeta} \sim \rho_m g \left(\frac{r_o}{r}\right)^2 \left(\frac{\partial z}{\partial x}\right)_{\zeta_o}.$$

This approximation significantly reduces the horizontal and vertical averaging in the C-grid staggering discretization of the correction term, and we have found that errors in resting atmosphere test simulations are reduced. Since the nonhydrostatic contributions to pressure are a small fraction of the hydrostatic pressure, this representation appears to maintain good accuracy.

The vertical momentum equation (7) is cast as

$$\begin{aligned}\frac{\partial W}{\partial t} = &-\overline{\left(\frac{\rho_d}{\rho_m}\right)}^{\zeta} \left[\tilde{r}_\omega^2 \frac{\partial p}{\partial \zeta} + g \overline{\left(\frac{\tilde{\rho}_m}{\tilde{r}_c^2}\right)}^{\zeta}\right] - (\nabla \cdot \mathbf{V} w)_\zeta \\ &+ \tilde{r}_\omega^2 \beta_d \overline{\left(\frac{\tilde{\rho}_d}{\tilde{r}_c^2}\right)}^{\zeta} \left[\frac{u_c^2 + v_c^2}{r} + e(u \cos\alpha_r - v_c \sin\alpha_r)\right] + \tilde{r}_\omega^2 F_W.\end{aligned} \tag{22}$$

The cell-centered horizontal velocities u_c and v_c in (22) are the cell-centered longitudinal and latitudinal velocities that are computed using a radial basis reconstruction (Bonaventura et al. 2011).

As with the definitions for $\tilde{\rho}$ and U, the operators (19) and (20) and the momentum equations (21) and (22) revert to their shallow-atmosphere form when $\tilde{r} = 1$ and $\beta_d = 0$.

MPAS-A uses a split explicit time integration technique whereby a smaller time step is used with a perturbation form of the governing equations to integrate the acoustic and gravity wave modes (see Klemp et al. 2007). The perturbations are defined relative to the values of the prognostic variables at the start of the current time step and are denoted by the $''$ superscript. The pressure gradient terms in the momentum equations, cast in terms of pressure p in (21) and (22), are recast in terms of a prognostic perturbation variable $\Theta'' = (\tilde{\rho}\theta)''$ to allow for the implicit time integration of the vertically propagating acoustic modes. The deep-atmosphere perturbation momentum equations for the split acoustic steps are

$$\frac{\partial U''}{\partial t} = -\tilde{r}_e \overline{\left(\frac{\rho_d^t}{\rho_m^t}\right)}^e \left[\frac{1}{\tilde{r}_e} \gamma R_d \overline{\pi^t}^e \frac{\partial}{\partial x}\left(\frac{\Theta_m''^\tau}{\tilde{r}_c^2}\right)\bigg|_{\zeta_o} + \overline{\left(\frac{\tilde{\rho}_d''}{\tilde{r}_c^2}\right)}^e g \frac{1}{\tilde{r}_e^3}\left(\frac{\partial z}{\partial x}\right)_{\zeta_o} \right] + \tilde{r}_e R_U^t, \tag{23}$$

$$\frac{\partial W''}{\partial t} = -\overline{\left(\frac{\rho_d^t}{\rho_m^t}\right)}^\zeta \left[\gamma R_d \overline{\pi^t}^\zeta \tilde{r}_\omega^2 \frac{\partial\left(\zeta_z \overline{\Theta_m''}^\tau / \tilde{r}_c^2\right)}{\partial \zeta} - g \frac{R_d}{c_v} \overline{\left(\frac{\tilde{\overline{\rho}}_d^t}{\tilde{r}_c^2}\frac{\pi'}{\overline{\pi}}\frac{\overline{\Theta_m''}^\tau}{\Theta_m^t}\right)}^\zeta \right] - g \overline{\left(\frac{\tilde{\rho}_d''}{\tilde{r}_c^2}\right)}^{\zeta\tau} + \tilde{r}_\omega^2 R_W^t, \tag{24}$$

where $\gamma = c_p/c_v$ is the ratio of the dry-air heat capacities at constant pressure and volume, and π is the Exner function. τ represents the integration time during the acoustic substeps in the time-split scheme for the current full time step beginning at time t. The operator $\overline{(\,)}^\tau$ represents a time average over the acoustic time step in the acoustic step vertical momentum equation (24). As with the other equations, the perturbation equations (23) and (24) revert to their shallow-atmosphere form when $\tilde{r} = 1$.

In the discrete conservation equation for cell-centered variables (12), the terms $\overline{b}^e$ and $\overline{b}^\zeta$ denote projections of b (where b may be a mixing ratio, θ_m, or ρ_d) onto the cell faces, where the formulation of the projections determine the order of accuracy of the scheme. The operator $\overline{(\,)}^e$ in (21) and (23) represents horizontal (along coordinate surfaces) projections to cell edges from the cell centers, and here are accomplished by taking an average of the cell center values from the two cells owning the edge. Edges bisect the lines connecting cell centers, so this also corresponds to a linear interpolation. The operator $\overline{(\,)}^\zeta$ in (21)–(24) represents vertical projections from cell interfaces (w point) to the cell centers or from cell centers to a cell interface in the vertical momentum equations (22) and (24). Projections from w points to cell-center points are computed as averages because cell centers are located halfway between the w points in both the physical space z and computational space ζ.

MPAS-A often employs a vertical mesh that is not uniform, and in this case the w points do not lie halfway between cell centers. MPAS-A (and WRF; Skamarock et al. 2019) have used linear interpolation in the computational ζ space to project cell-centered values to the w points, thus maintaining spatial second-order accuracy for the buoyancy term in the vertical momentum equation discretization. In examining energy conservation for the discrete system, we found a small but noticeable error that was significantly reduced when we changed this projection to represent the integrated average value between the cell centers. The piecewise constant distribution of density and potential temperature is consistent with their definition within the finite-volume formulation as cell-averaged values, and is consistent with the integrals of the potential, internal, and kinetic energy for MPAS. Assuming a piecewise constant distribution in a cell, the weights for the integrated average value are reversed from those of the linear interpolation. We find little discernible difference in the solutions using either approach. MPAS-A does not exactly conserve total energy, and this modification results in a very small reduction in the total energy budget residual.

As noted earlier, the shallow-atmosphere solver in the MPAS implementation is recovered simply by setting the $\tilde{r}$ coefficients to 1 and β_d to zero (disabling the additional Coriolis and curvature terms appearing in the deep-atmosphere formulation). Tests with the unmodified MPAS-Atmosphere version 7 release and the deep-atmosphere-enabled version 7 indicate that the additional terms and operations in the deep-atmosphere code increase the cost of the dry dynamics by less than 5%. The inclusion of moisture and model physics would substantially reduce this overhead. No effort has been made to optimize the implementation of the additional operations.

3. Baroclinic waves on the Earth-radius sphere

There exist only a few published idealized tests for atmospheric fluid-flow solvers employing the deep-atmosphere equations. In Ullrich et al. (2014), solutions from shallow and deep-atmosphere solvers are evaluated for the case of an unstable baroclinic jet on both an Earth-radius sphere and a reduced-radius sphere. For the Earth-radius sphere, solutions produced with solvers employing the shallow-atmosphere equations are very similar to the deep-atmosphere solutions. We present Earth-radius sphere solutions for this test using the deep-atmosphere version of MPAS in this section, and examine additional aspects of the solution not discussed in Ullrich et al.

The unstable baroclinic wave case in Ullrich et al. begins with an initial state that does not vary zonally. The initial states for both the shallow and deep equations are analytic, and represent steady state solutions (in geostrophic and hydrostatic balance for both the shallow and deep equations) in the absence of perturbations to the jets. The initial states have constant surface pressure (1000 hPa) and zero wind speed at the surface. There is no terrain in this test configuration and the model top (a rigid lid in the case of MPAS) is set at 30 km. A full description of the analytic initial states for both shallow

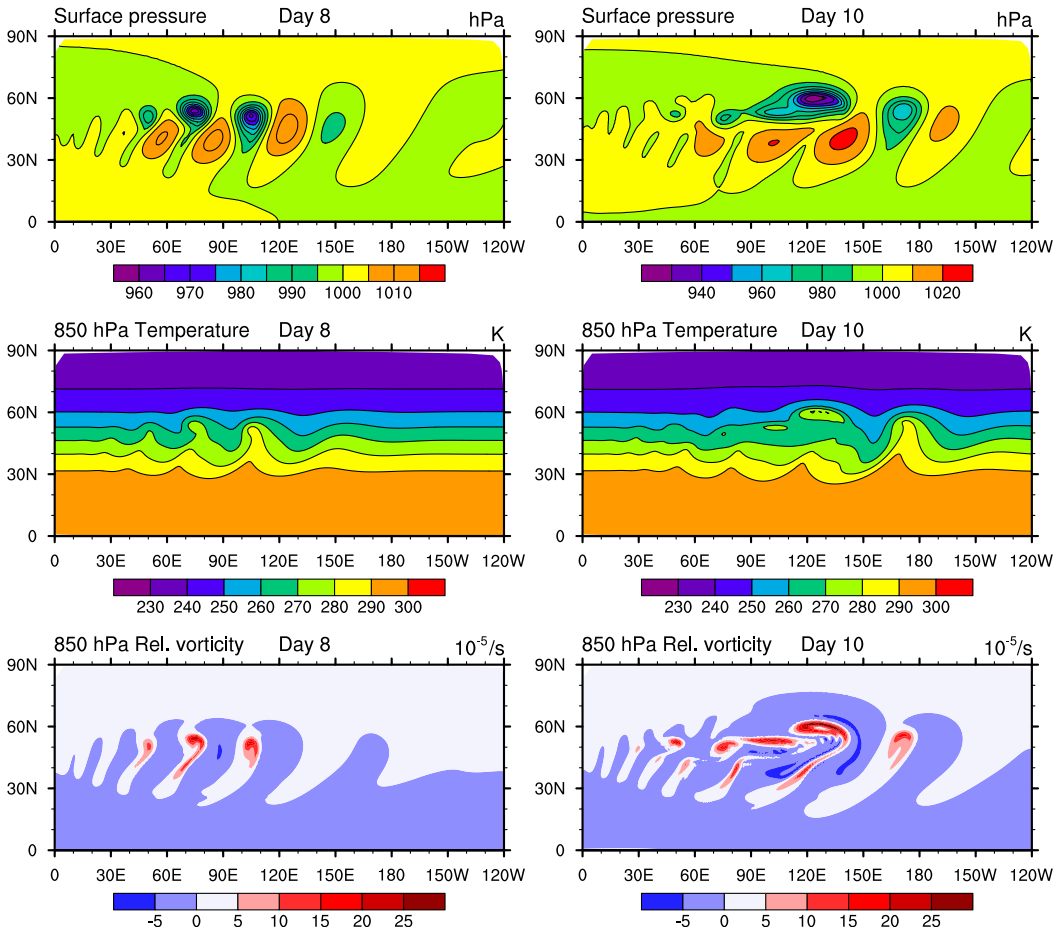

FIG. 2. Results from the MPAS deep-atmosphere simulation for the Earth-radius sphere. These can be compared directly with the MCore and EndGame model results in Ullrich et al.'s (2014) Figs. 4 and 5.

and deep-atmosphere equations is found in Ullrich et al. (2014), and the code used to produce the initial states is that used in the 2016 Dynamical Core Model Intercomparison Project (DCMIP, Ullrich et al. 2018). For the MPAS initialization we specify height and latitude as inputs and use the output temperature profile at model levels along with the surface pressure to compute a thermodynamic profile that satisfies the discrete hydrostatic balance and state equation within MPAS. In the deep-atmosphere case the hydrostatic balance also accounts for the deep-atmosphere Coriolis and curvature terms and the dependence of gravity on height. The zonal velocities are pointwise specified (evaluated at the face centers), and no special treatment is used to remove initial horizontal divergence. The initial perturbation used to trigger the baroclinic waves is specified within the DCMIP-based initialization code, and we use the same perturbation as described by Ullrich et al. We employ the same vertical mesh as used in Ullrich et al. [2014, Eq. (28)] and a quasi-uniform horizontal Voronoi mesh with approximately 120-km cell-center spacing is used for these tests. The reference solutions from MPAS use the standard configuration from the MPAS version 7 release for model filters, including the fourth-order horizontal background hyperviscosity, a Smagorinsky-based second-order horizontal filter, and upwind biased transport settings.

Plots at days 8 and 10 of the surface pressure and 850-hPa temperature and relative vorticity from the deep-atmosphere MPAS integrations for the baroclinic wave integration on the Earth-radius sphere are given in Fig. 2, and can be directly compared with results from Ullrich et al. (2014; their Figs. 4 and 5) from the MCore model and the Met Office ENDGame model, respectively (see Ullrich et al. for details concerning these models). The results from the three models are very similar, with only minor differences in the small-scale structure (e.g., the vorticity filaments). The deep-atmosphere solutions are also similar to shallow-atmosphere model integrations for MPAS (not shown) and shallow-atmosphere results presented in Ullrich et al. The similarity of the shallow and deep results is expected given that the ratio of the domain depth to Earth's radius is small (~1/200).

We also find similar evolution of the minimum surface pressure depicted in Fig. 3 where both the MPAS and Ullrich et al. results are shown. Frontal collapse occurs between days 8 and 9 in the simulation, and it is in the period following collapse that we observe some spreading of the minimum pressures.

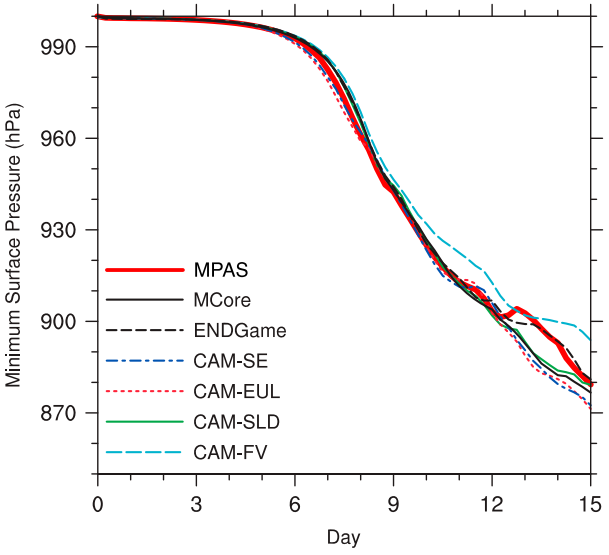

FIG. 3. Minimum surface pressure from the MPAS deep-atmosphere simulation plotted with those from the simulations presented in Ullrich et al.'s (2014) Fig. 7.

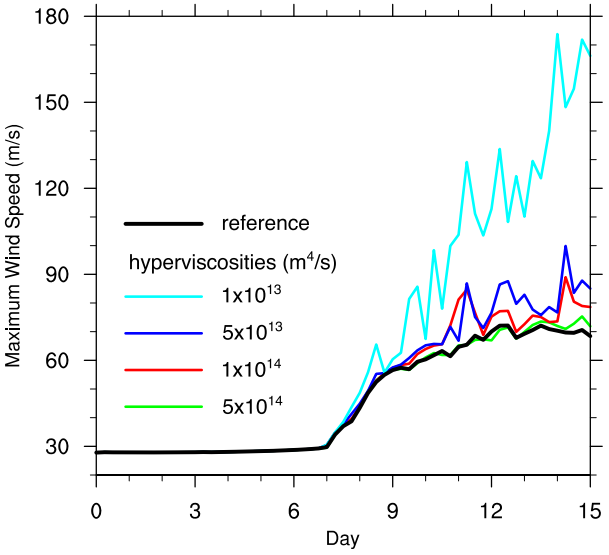

FIG. 4. Maximum horizontal wind speed from the MPAS deep-atmosphere results using different values for the hyperviscosity. The reference solution uses the default MPAS dissipation configuration, while for the hyperviscosity results all other spatial filters are disabled.

The MPAS surface pressure results are relatively insensitive to the MPAS configuration details (e.g., time step, filter configuration), and the small differences are confined to the period after day 12.

While the surface pressure is relatively insensitive to the filtering configurations in MPAS, the maximum wind speed for the MPAS simulations, given in Fig. 4, shows significant sensitivity to the MPAS filtering configuration. This baroclinic wave test uses free-slip lower and upper boundaries, and the maximum wind speed is located within the jet core until day 7 after which it is found at the lowest (i.e., near-surface) model level. Aside from the default dissipation configuration used in the reference simulation, the horizontal fourth-order filter is the only active spatial filter in these hyperviscosity tests (i.e., the MPAS second-order Smagorinsky filter, and upwinding in the transport operators, are disabled). The highest value of the hyperviscosity used in these simulations ($5 \times 10^{14}\,\mathrm{m^4\,s^{-1}}$) is the value used by the CAM-EUL and CAM-SE models in integrations presented in Ullrich et al. (2014). The MCore, ENDGame, and CAM-FV models rely on dissipation inherent in the discretization (e.g., in the transport operators, etc.). The maximum velocities increase with decreasing hyperviscosity in MPAS with the least-filtered configuration producing results having values over twice as high as that produced by the most-filtered configuration. There is also more finescale structure in the vorticity fields along with larger values (not shown) in the MPAS simulations when the hyperviscosity is reduced. Given that there is no fixed physical viscosity or hyperviscosity in the test case specification, the solution cannot be converged and there is no quantitative measure of model error. The largest solution differences among different models is as likely due to the differing filter configurations and damping implicit in the formulations as it is to the different base discretizations, grid staggerings employed, etc.

MPAS has been designed to conserve mass and scalar mass, but it has not been designed to conserve total energy. The integration of mass over the MPAS mesh can be expressed as

$$M = \sum_{\text{cells}} \rho V_{\text{cell}} = \sum_{\text{cells}} \rho A_o \Delta z \tilde{r}_c^2 . \tag{25}$$

MPAS uses a cell-centered approximation for the horizontal kinetic energy (KE) in the discretization of the horizontal

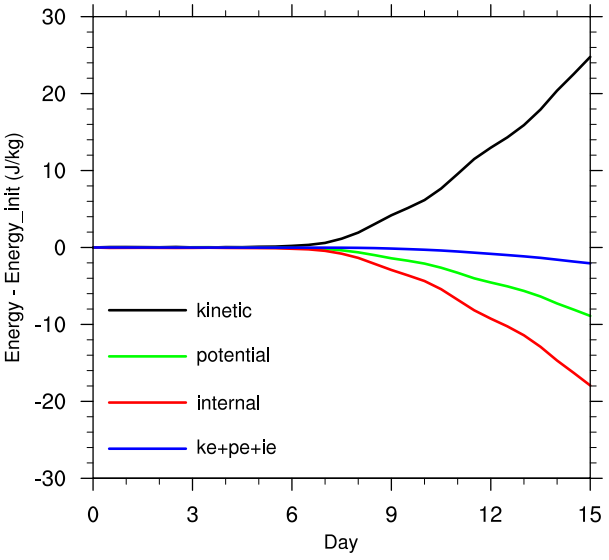

FIG. 5. Energy budget for the MPAS deep-atmosphere reference simulation. For reference, the initial kinetic energy is approximately $77.5\,\mathrm{J\,kg^{-1}}$.

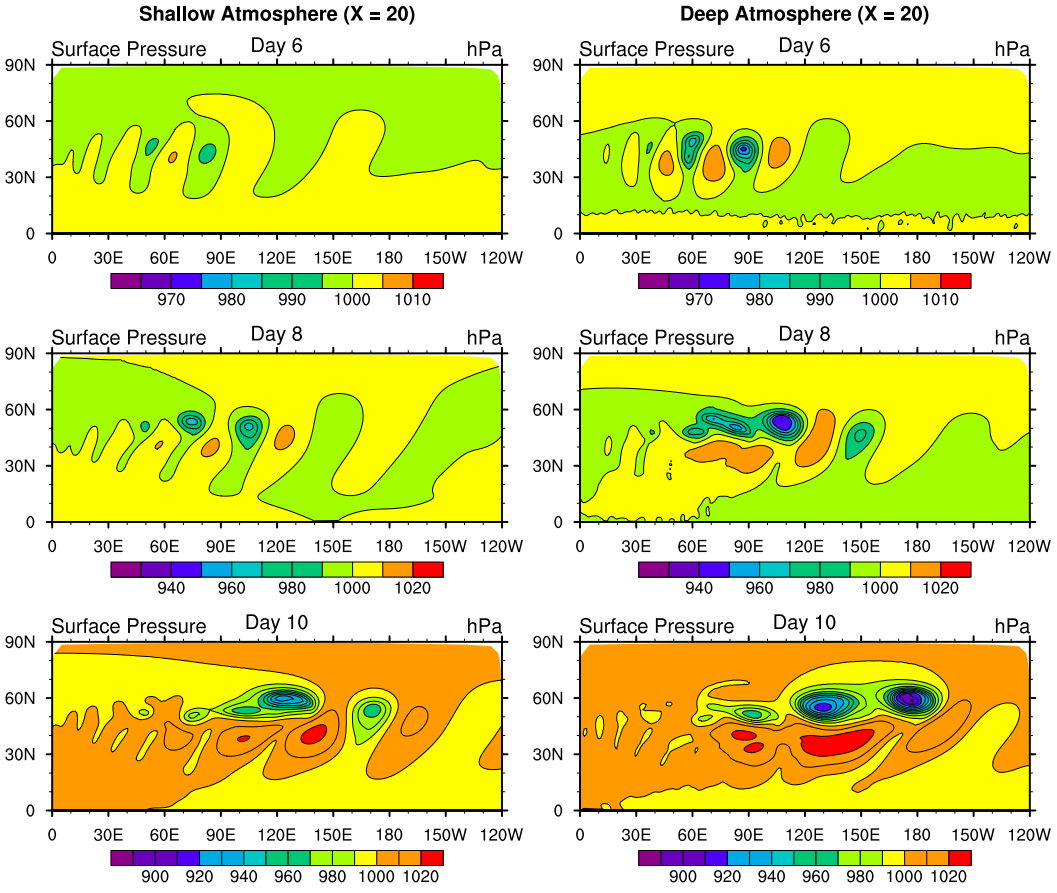

FIG. 6. MPAS surface pressure fields at days 6, 8, and 10 for the shallow- and deep-atmosphere jet simulations for the X20 reduced-radius sphere test cases. These can be compared directly with Fig. 9 in Ullrich et al. (2014), and with the deep-atmosphere solutions at days 8 and 10 from the ICON model in Borchert et al.'s (2019) Fig. 6.

momentum equation (21), while the vertical velocity is prognosed at the layer interfaces. We integrate the horizontal KE over the domain in a similar manner to mass. For the vertical component we evaluate w^2 at the interfaces and weight the density to those interfaces as is done for the density term in the vertical momentum equation, and then integrate over the volume extending vertically from the cell centers below and above the w interface point. Using this formulation the KE integral can be expressed as

$$\mathrm{KE} = \sum_{\text{cells}} (\rho \mathrm{KE}_h) A_o \tilde{r}_c^2 \Delta z + \sum_{w\,\text{cells}} \left(\overline{\rho}^z \frac{w^2}{2} \right) A_o \tilde{r}_\omega^2 \Delta z_\omega . \tag{26}$$

The internal energy is computed as

$$\mathrm{IE} = \sum_{\text{cells}} \rho c_v T A_o \Delta z \tilde{r}_c^2 . \tag{27}$$

The potential energy is expressed as

$$\mathrm{PE} = \sum_{\text{cells}} \rho g \left(z + \frac{z^2}{r_0} \right) A_o \Delta z . \tag{28}$$

The time evolution of the total energy and its components for the Earth-radius sphere results are given in Fig. 5. The kinetic energy increases over time as the wave develops, and the potential and internal energy decrease. The initial kinetic energy normalized by the atmospheric mass is 77.5 J kg^{-1}, so the kinetic energy increases by approximately one-third from its original value over the 15 day integration. The total energy decreases slightly over time starting around day 8. The dissipation of kinetic energy is not added back into the internal energy in this configuration of MPAS, so the decrease in total energy is expected and could be used as an estimate of the kinetic energy dissipation. Because MPAS is not designed to conserve total energy, the change in total energy could also occur because of discretization-based errors relative to energy conservation in the scheme, but qualitatively the energetics of the MPAS deep-atmosphere formulation are behaving properly.

4. Baroclinic waves on the reduced-radius sphere

The baroclinic wave solutions on the Earth-radius sphere are very similar for the shallow and deep-atmosphere equation solvers. Ullrich et al. (2014) also present results from tests of the MCore model using a reduced-radius sphere, in their case reducing the sphere radius by a factor of 20 and raising the

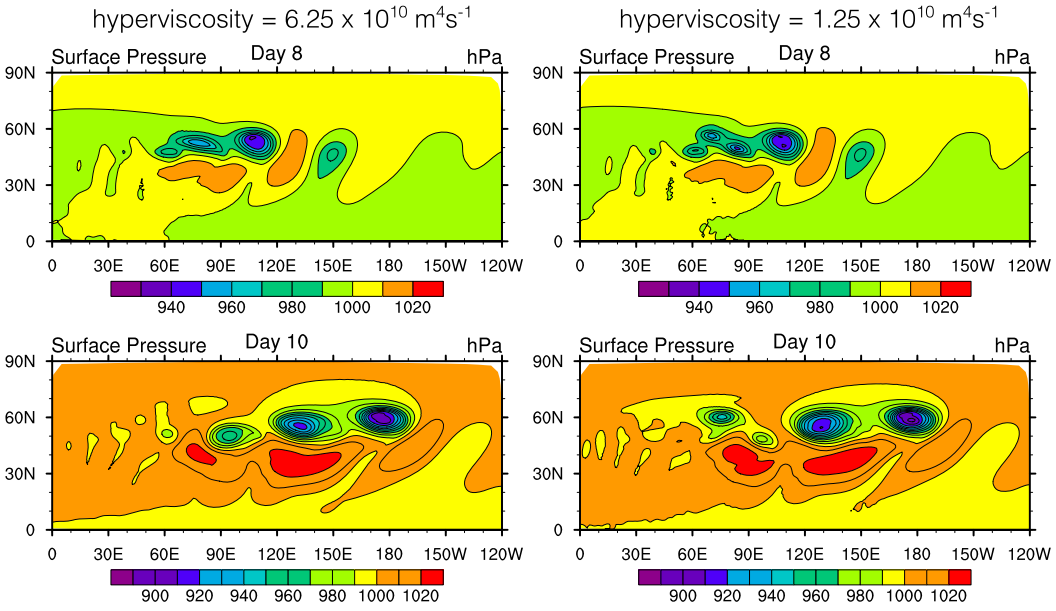

FIG. 7. Surface pressure fields at days 8 and 10 for the deep-atmosphere jet simulations for the X20 reduced-radius sphere test case using two values of a fixed hyperviscosity. The results in the left panels are very similar to the MCore results in Ullrich et al.'s (2014) Fig. 9 and to the $\Delta\varphi = 0.95°$ mesh results in Borchert et al.'s (2019) Fig. 6 (top panels). The results in the right panels are very similar to the $\Delta\varphi = 0.48°$ mesh results in Borchert et al.'s (2019) Fig. 6 (middle panels).

rotation rate of the sphere by a factor of 20 (Ullrich et al. label this the X20 case). The evolutions of the baroclinic waves for this reduced-radius sphere tests are very different in the shallow and deep equations solutions. We have repeated these test simulations with MPAS and display in Fig. 6 the shallow- and deep-atmosphere surface pressure fields at days 6, 8, and 10. These results can be compared with Fig. 9 in Ullrich et al. (2014) showing results from MCore, and the deep-atmosphere results for days 8 and 10 can be compared with Fig. 6 in Borchert et al. (2019) for the ICON model. The shallow and deep-atmosphere solutions are quite similar in the MCore and MPAS results, and the deep-atmosphere results from ICON are similar to those from MCore and MPAS. The differences between the shallow and deep-atmosphere structure are very pronounced at days 6 and 8 where the deep-atmosphere wave has much more amplitude and structure compared to the shallow-atmosphere solution. There is also small-scale structure that could be characterized as noise in the equatorial region of the ICON and MPAS solutions. We also find that the MPAS solutions are insensitive to increased vertical resolution (i.e., above the baseline 30 levels), confirming the ICON-based results reported in Borchert et al. (2019).

The primary differences in the reduced-radius deep-atmosphere test case results in Ullrich et al. (2014), Borchert et al. (2019), and those reported here are found in the smaller-scale low pressure disturbances trailing (to the west of) the main baroclinic waves, specifically the waves between 60° and 90°E on day 8 and those west of 120°E on day 10 in Fig. 6. We have found that one significant source of these differences are the dissipation and model stabilization techniques and configurations employed in the models. For example, MCore does not apply explicit filters in its formulation, rather the filtering is implicit in its formulation. ICON includes explicit filters in its formulation in addition to filtering implicit in its transport scheme formulation, and MPAS follows a similar approach employing both explicit and implicit filtering in its default configuration. Figure 7 depicts the surface pressure at days 8 and 10 from two additional MPAS simulations for the reduced-radius deep-atmosphere test case where the explicit spatial filters were disabled except for the fourth-order horizontal hyperviscosity formulation. Two different fixed values of the hyperviscosity were used, 6.25×10^{10} and $1.25 \times 10^{10}\,\mathrm{m^4\,s^{-1}}$, and these correspond to values of 5×10^{14} and $1 \times 10^{14}\,\mathrm{m^4\,s^{-1}}$ scaled by the sphere radius reduction cubed (1/8000). The results using the larger hyperviscosity, depicted in the left panels, compare very well with the MCore solution shown in Ullrich et al.'s Fig.9, especially for day 8. The right panels depict the solution employing a hyperviscosity with 1/5 the magnitude, and these results compare very well with the ICON results given in Borchert et al.'s Figs. 6c and 6d that are computed on a mesh with twice the horizontal mesh density ($\Delta\varphi = 0.48°$, ~53 km) than that reported for MCore (1°) and MPAS ($\Delta x \sim$ 120 km). These tests confirm that the specifics of a model's configuration, in this case the filter configuration, play a significant role in this intercomparison, and that it is possible to tune model configurations to produce specific structures, in this case structures in the trailing baroclinic waves. The results also further illustrate the lack of convergence in the solutions that was also shown previously in the Borchert et al. results.

Figures 8a and 8b show the zonal wind fields and the potential temperature for the shallow and deep-atmosphere initial state jets in a meridional cross section. The midlatitude jet

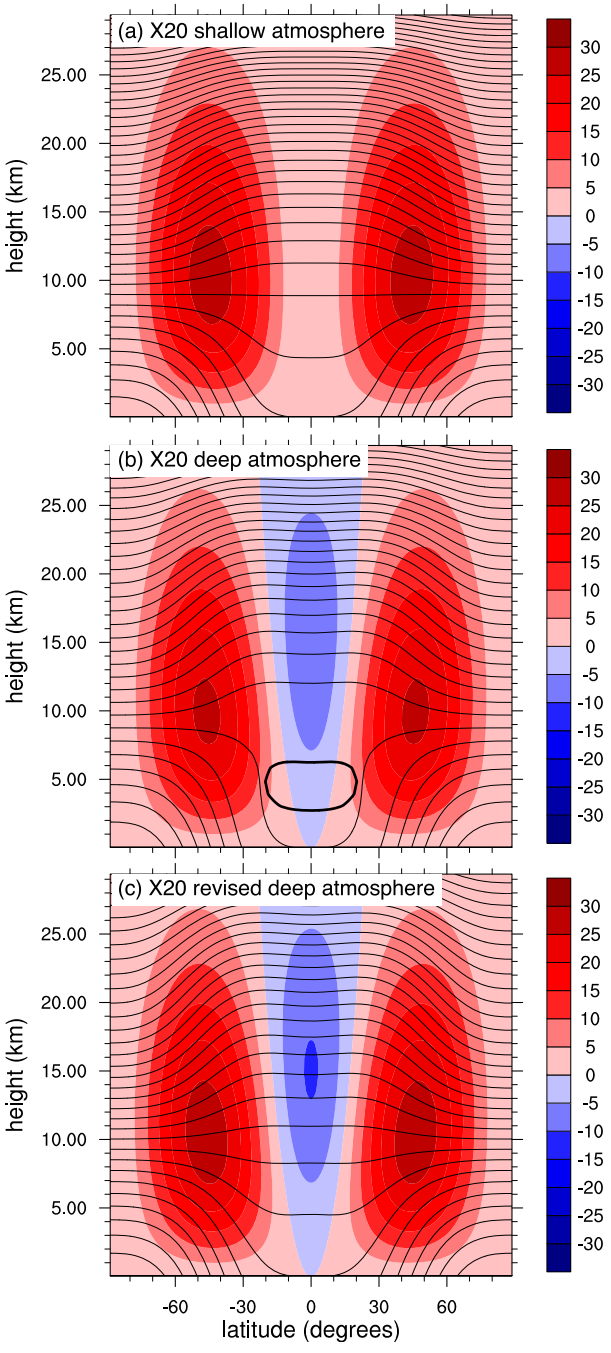

FIG. 8. Cross sections for the initial states used in the X20 reduced-radius sphere tests. Colors are the zonal velocity (m s^{-1}), thin black contours are potential temperature (K) with a 10-K contour interval, and the thick contour indicates absolute instability ($\theta_z < 0$).

in the shallow-atmosphere state is both wider and deeper than that in the deep-atmosphere state. There also exists an easterly equatorial jet in the deep-atmosphere initial state that is entirely absent from the shallow-atmosphere state. Perhaps most notable is the region with unstable lapse rates ($\theta_z < 0$) in the tropics in the lower troposphere between approximately 3 and 6 km. Further examination of the MPAS deep-atmosphere solution indicates that the small-scale structure appears to be related to this layer overturning as disturbances reach it and trigger the instability.

The equatorial lower-tropospheric instability in the analytic deep-atmosphere initial state for the X20 reduced-radius sphere can be removed by increasing the reference temperature T_o from the value $T_o = (T_o^e + T_o^p)/2 = 275$ K [Ullrich et al. 2014, their Eq. (18)], where $T_o^e = 310$ K is surface temperature at the equator and $T_o^p = 240$ K is the surface temperature at the poles, to a higher value (P. Ullrich 2020, personal communication). We have found that using $T_o = 0.8T_o^e + 0.2T_o^p = 296$ K for the X20 deep-atmosphere case removes the unstable lapse rates and produces a lower-tropospheric lapse rate at the equator similar to that found in the shallow-atmosphere initial state using the Ullrich et al. value of 275 K. This alternative deep-atmosphere initial state is given in Fig. 8c. One interesting artifact of this modification is the strengthening of the equatorial easterly jet compared with the original deep-atmosphere initialization. In both cases absolute geostrophic vorticity $\zeta_g + f$ is positive everywhere in the initial state, thus neither deep-atmosphere states for the X20 jet are inertially unstable even with the enhanced negative relative vertical vorticity associated with the easterly equatorial jet.

Results from this revised deep-atmosphere initial state for the X20 reduced-radius sphere are given in Fig. 9, and the shallow-atmosphere results are plotted again in this figure for direct comparison. The shallow- and deep-atmosphere solutions are remarkably similar and there is no longer any significant small-scale structure in the equatorial region. These results strongly indicate that the unstable layer was the source of the equatorial noise in the original X20 deep-atmosphere jet, and that the major differences between the shallow and deep-atmosphere solutions presented in Ullrich et al. (2014) for MCore and for the corresponding MPAS results presented in Fig. 6 are primarily the result of differences in the initial state and not directly the result of the temporal integration of the shallow and deep equations using these states.

5. Summary and discussion

We have presented an extension of the shallow-atmosphere equations solver used in MPAS that enables the integration of the deep-atmosphere equations. For cell-based variables (ρ, θ, q), the deep-atmosphere geometry is accounted for by modifying the coordinate metric terms in the coupled density and momentum variables (16)–(18) that were already present in the shallow-atmosphere solver; thus the flux-divergence operators and time integration code are identical in both systems and a single integration code is shared by both equation sets. Additional coefficients are required in the momentum equations to accommodate the deep-atmosphere formulation, and they are cast as ratios of the radial distance of points from the center of the sphere to the sphere radius. In this implementation, setting these coefficients to 1 and disabling the deep-atmosphere Coriolis and curvature terms is all that is needed to integrate the shallow-atmosphere equations in the

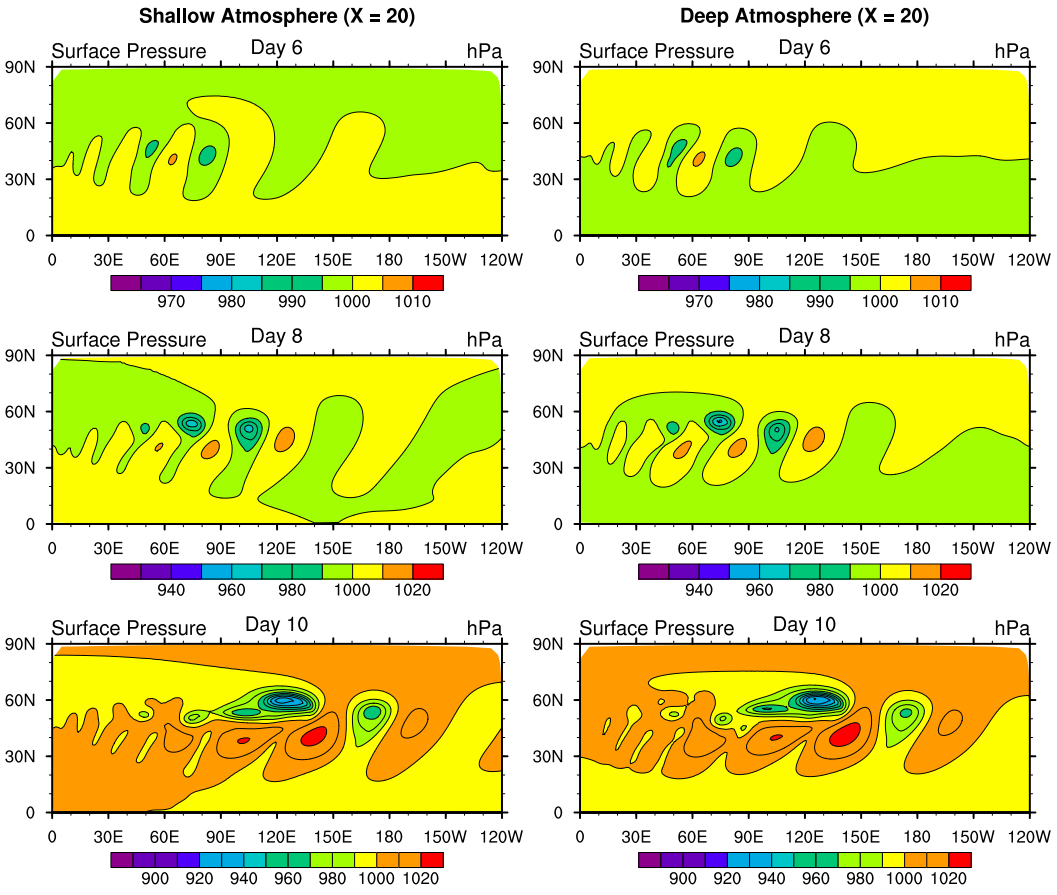

FIG. 9. Surface pressure fields at days 6, 8, and 10 for the shallow- and deep-atmosphere jet simulations for the X20 reduced-radius sphere test cases with the revised deep-atmosphere initial state that removes the absolute instability.

deep-atmosphere-enabled MPAS code. Tests with the MPAS version 7 release and the deep-atmosphere enabled version 7 show that the additional cost of the dry dynamics is less than 5% as indicated in timings for the tests presented in this paper.

Idealized baroclinic wave test cases for an Earth-radius sphere and a reduced-radius sphere (the X20 case of Ullrich et al. 2014) are carried out to examine the performance of the deep-atmosphere extension of MPAS. The shallow and deep-atmosphere solutions from MPAS are similar to other model results for these same tests as reported in Ullrich et al. (2014) and in Borchert et al. (2019). We found that the evolution of domain-maximum horizontal velocity is much more sensitive to model configuration compared to the minimum surface pressure for the Earth-radius sphere experiments, of which the latter is most often cited in the literature, e.g., Ullrich et al. (2014). We also examined energy conservation in the solutions as an additional metric not examined in any of the other studies. Even though MPAS has not been designed to conserve energy, the total energy and its components evolve as expected.

The deep-atmosphere reduced-radius sphere (X20) test case exhibited the most significant differences in the surface pressure fields in model simulation comparisons, in this case in the smaller-scale baroclinic waves. We found that the different structures reported by others could be produced in MPAS by modifying the dissipation configuration.

In this study and in other published results, the X20 deep-atmosphere solutions are markedly different than X20 shallow solutions. We found one significant issue with the deep-atmosphere X20 test case initial analytic state given in Ullrich et al. (2014). This initial state contains unstable lapse rates ($\theta_z < 0$) in the equatorial lower-troposphere that lead to small-scale structure (noise) as a result of overturning in the equatorial region in the evolving solution. A simple adjustment to the X20 deep-atmosphere initial state specification produces equatorial tropospheric lapse rates similar to those in X20 shallow-atmosphere initial state. Simulations using the revised deep-atmosphere initial state result in similar evolution of the X20 deep and X20 shallow states and removes the equatorial noise from the deep-atmosphere evolution. These results indicate that the differences in the X20 deep and shallow solutions reported in Ullrich et al. (2014), and reproduced here and in Borchert et al. (2019), arise primarily because of differences in the initial states and not primarily from integrating the deep versus shallow equations. Unfortunately, these results also reveal that this reduced-radius sphere test case is not very

discriminating for use in evaluating the numerics of the deep-atmosphere equations.

Test cases for atmospheric models, in order to be useful, should have clear measures of solution correctness and allow for the diagnosis of the source of model errors when incorrect solutions are produced, the latter typically through some understanding of the critical terms in the equations where discretization errors are likely to lead to errors in the simulated flows. The similarity between solutions from different models provides evidence of solution correctness for the baroclinic wave test cases used in this study. Of note, our experience implementing the deep-atmosphere extension in MPAS is that the model's ability to maintain the initial balance (both hydrostatic and geostrophic) in the analytic initial state was most useful in finding and removing discretization or formulation errors, while the simulations provided further verification but little additional information to guide the implementation. The initial state balances for the deep and shallow-atmosphere initializations are the only analytic solutions we have for the full model equations. Additionally, given the similarity between the shallow and deep X20 reduced-radius sphere solutions for similar initial states, we cannot easily gauge the effects of the additional deep-atmosphere terms when comparing different solutions.

Further work is needed to develop tests that allow for unambiguous evaluation of nonhydrostatic deep-atmosphere solvers and that provide for quantitative assessment of the impact of the shallow-atmosphere approximation. There have been a number of efforts to develop test cases following the approach of Wedi and Smolarkiewicz (2009) where a reduced-radius sphere is used to lower computational cost for higher horizontal-resolution testing. For the tests considered here, the balanced initial jet states for the shallow and deep equations cannot be identical because they satisfy different balance constraints, thus there is no straightforward way to identify solution differences that arise from the different initial states and those that arise from integrating different evolution equations. Thus the comparisons are only qualitative at this stage, and they do not directly address the question of when the shallow-atmosphere approximation becomes problematic. We appreciate that this is not an entirely satisfactory way to evaluate the correctness of models nor the validity of equation sets.

The extensions to the MPAS dynamical core presented in this paper address the deep-atmosphere geometry and the full Coriolis and curvature terms. These are necessary steps in the evolution of this nonhydrostatic solver to applications requiring higher model tops. We have not addressed important changes needed within atmospheric physics components, for example the extension of the plane-parallel radiation flux to include the spherical metrics. For geospace applications, where the model top may extend to 500 km or more above Earth's surface, additional capabilities will be needed, including a generalization of the equation of state to include evolving prognostic atmospheric constituents, additional prognostic equations for those constituents, and methods to integrate the viscous terms given the high physical viscosities characterizing the upper atmosphere. We will report on these extensions in future work.

Acknowledgments. Funding for this research was provided by the National Center for Atmospheric Research through support from the National Science Foundation under Cooperative Support Agreement AGS-0856145. Author Hing Ong was funded under a Taiwanese Ministry of Education Government Scholarship to Study Abroad.

REFERENCES

Akmaev, R. A., 2011: Whole atmosphere modeling: Connecting terrestrial and space weather. *Rev. Geophys.*, **49**, RG4004, https://doi.org/10.1029/2011RG000364.

Bonaventura, L., A. Iske, and E. Miglio, 2011: Kernel-based vector field reconstruction in computational fluid dynamic models. *Int. J. Numer. Methods Fluids*, **66**, 714–729, https://doi.org/10.1002/fld.2279.

Borchert, S., G. Zhou, M. Baldauf, H. Schmidt, G. Zängl, and D. Reinert, 2019: The upper-atmosphere extension of the ICON general circulation model (version: ua-icon-1.0). *Geosci. Model Dev.*, **12**, 3541–3569, https://doi.org/10.5194/gmd-12-3541-2019.

Dickinson, R. E., E. C. Ridley, and R. G. Roble, 1981: A three-dimensional general circulation model of the thermosphere. *J. Geophys. Res. Space Phys.*, **86**, 1499–1512, https://doi.org/10.1029/JA086iA03p01499.

Glatzmaier, G. A., M. Evonuk, and T. M. Rogers, 2009: Differential rotation in giant planets maintained by density-stratified turbulent convection. *Geophys. Astrophys. Fluid Dyn.*, **103**, 31–51, https://doi.org/10.1080/03091920802221245.

Harris, M. J., N. F. Arnold, and A. D. Aylward, 2002: A study into the effect of the diurnal tide on the structure of the background mesosphere and thermosphere using the new coupled middle atmosphere and thermosphere (CMAT) general circulation model. *Ann. Geophys.*, **20**, 225–235, https://doi.org/10.5194/angeo-20-225-2002.

Hayashi, M., and H. Itoh, 2012: The importance of the nontraditional Coriolis terms in large-scale motions in the tropics forced by prescribed cumulus heating. *J. Atmos. Sci.*, **69**, 2699–2716, https://doi.org/10.1175/JAS-D-11-0334.1.

Heimpel, M., J. Aurnou, and J. Wicht, 2005: Simulation of equatorial and high-latitude jets on Jupiter in a deep convection model. *Nature*, **438**, 193–196, https://doi.org/10.1038/nature04208.

Klemp, J. B., 2011: A terrain following coordinate with smoothed coordinate surfaces. *Mon. Wea. Rev.*, **139**, 2163–2169, https://doi.org/10.1175/MWR-D-10-05046.1.

——, W. C. Skamarock, and J. Dudhia, 2007: Conservative split-explicit time integration methods for the compressible nonhydrostatic equations. *Mon. Wea. Rev.*, **135**, 2897–2913, https://doi.org/10.1175/MWR3440.1.

Liu, H.-L., and Coauthors, 2018: Development and validation of the Whole Atmosphere Community Climate Model with thermosphere and ionosphere extension (WACCM-X 2.0). *J. Adv. Model. Earth Syst.*, **10**, 381–402, https://doi.org/10.1002/2017MS001232.

Müller, R., 1989: A note on the relation between the "traditional approximation" and the metric of the primitive equations. *Tellus*, **41A**, 175–178, https://doi.org/10.1111/j.1600-0870.1989.tb00374.x.

Ong, H., and P. E. Roundy, 2019: Linear effects of nontraditional Coriolis terms on intertropical convergence zone forced large-scale flow. *Quart. J. Roy. Meteor. Soc.*, **145**, 2445–2453, https://doi.org/10.1002/qj.3572.

——, and ——, 2020a: Nontraditional hypsometric equation. *Quart. J. Roy. Meteor. Soc.*, **146**, 700–706, https://doi.org/10.1002/qj.3703.

——, and ——, 2020b: The compressional beta-effect: Analytical solution, numerical benchmark, and data analysis. *J. Atmos. Sci.*, **77**, 3721–3732, https://doi.org/10.1175/JAS-D-20-0124.1.

Ridley, A., Y. Deng, and G. Tóth, 2006: The global ionosphere-thermosphere model. *J. Atmos. Sol.-Terr. Phys.*, **68**, 839–864, https://doi.org/10.1016/j.jastp.2006.01.008.

Roble, R. G., E. C. Ridley, A. D. Richmond, and R. E. Dickinson, 1988: A coupled thermosphere/ionosphere general circulation model. *Geophys. Res. Lett.*, **15**, 1325–1328, https://doi.org/10.1029/GL015i012p01325.

Satoh, M., 2002: Conservative scheme for the compressible nonhydrostatic models with the horizontally explicit and vertically implicit time integration scheme. *Mon. Wea. Rev.*, **130**, 1227–1245, https://doi.org/10.1175/1520-0493(2002)130<1227:CSFTCN>2.0.CO;2.

——, T. Masuno, H. Tomita, H. Miura, T. Nasuno, and S. Iga, 2008: Nonhydrostatic Icosahedaral Atmospheric Model (NICAM) for global cloud resolving simulations. *J. Comput. Phys.*, **227**, 3486–3514, https://doi.org/10.1016/j.jcp.2007.02.006.

Skamarock, W. C., and A. Gassmann, 2011: Conservative transport schemes for spherical geodesic grids: High-order flux operators for ODE-based time integration. *Mon. Wea. Rev.*, **139**, 2962–2975, https://doi.org/10.1175/MWR-D-10-05056.1.

——, J. B. Klemp, M. G. Duda, L. D. Fowler, S.-H. Park, and T. Ringler, 2012: A multiscale nonhydrostatic atmospheric model using centroidal Voronoi tesselations and C-grid staggering. *Mon. Wea. Rev.*, **140**, 3090–3105, https://doi.org/10.1175/MWR-D-11-00215.1.

——, and Coauthors, 2019: A Description of the Advanced Research WRF Model version 4. NCAR Tech. Note NCAR/TN-556+STR, 145 pp., https://doi.org/10.5065/1dfh-6p97.

Thuburn, J., T. Ringler, W. C. Skamarock, and J. B. Klemp, 2009: Numerical representation of geostrophic modes on arbitrarily structured C-grids. *J. Comput. Phys.*, **228**, 8321–8335, https://doi.org/10.1016/j.jcp.2009.08.006.

Tort, M., and T. Dubos, 2014: Dynamically consistent shallow-atmosphere equations with a complete Coriolis force. *Quart. J. Roy. Meteor. Soc.*, **140**, 2388–2392, https://doi.org/10.1002/qj.2274.

Ullrich, P., T. Melvin, C. Jablonowski, and A. Staniforth, 2014: A proposed baroclinic wave test case for deep- and shallow-atmosphere dynamical cores. *Quart. J. Roy. Meteor. Soc.*, **140**, 1590–1602, https://doi.org/10.1002/qj.2241.

——, P. H. Lauritzen, K. Reed, C. Jablonowski, C. Zarzycki, J. Kent, R. Nair, and A. Verlet-Banide, 2018: ClimateGlobalChange/DCMIP2016: v1.0 (version v1.0). Zenodo, https://doi.org/10.5281/zenodo.1298671.

Verhoeven, J., and S. Stellmach, 2014: The compressional beta effect: A source of zonal winds in planets? *Icarus*, **237**, 143–158, https://doi.org/10.1016/j.icarus.2014.04.019.

Wedi, N. P., and P. K. Smolarkiewicz, 2009: A framework for testing global non-hydrostatic models. *Quart. J. Roy. Meteor. Soc.*, **135**, 469–484, https://doi.org/10.1002/qj.377.

White, A. A., and R. Bromley, 1995: Dynamically consistent, quasi-hydrostatic equations for global-models with a complete representation of the Coriolis-force. *Quart. J. Roy. Meteor. Soc.*, **121**, 399–418, https://doi.org/10.1002/qj.49712152208.

——, B. J. Hoskins, I. Roulstone, and A. Staniforth, 2005: Consistent approximate models of the global atmosphere: Shallow, deep, hydrostatic, quasi-hydrostatic and non-hydrostatic. *Quart. J. Roy. Meteor. Soc.*, **131**, 2081–2107, https://doi.org/10.1256/qj.04.49.

Wood, N., and Coauthors, 2014: An inherently mass-conserving semi-implicit semi-Lagrangian discretization of the deep- atmosphere global nonhydrostatic equations. *Quart. J. Roy. Meteor. Soc.*, **140**, 1505–1520, https://doi.org/10.1002/qj.2235.